ELSEVIER

Contents lists available at ScienceDirect

# Journal of Power Sources

journal homepage: www.elsevier.com/locate/jpowsour





# Quantifying key parameters to provide better understating of microstructural changes in polymer electrolyte membrane fuel cells during degradation: A startup/shutdown case study

Amir Peyman Soleymani <sup>a</sup>, Leonard Bonville <sup>a</sup>, Chunmei Wang <sup>b,1</sup>, Stephanie Schaefer <sup>b</sup>, James Waldecker <sup>b</sup>, Jasna Jankovic <sup>a,\*</sup>

#### HIGHLIGHTS

- Comprehensive microstructural characterization/quantification is executed on PEMFC.
- Microstructural descriptors are related to degradation and performance in SUSD.
- Microstructural degradation of unprotected SUSD was in line with performance loss.
- Microstructural descriptors confirmed minor degradation in protected SUSD.

#### ARTICLE INFO

# Keywords: Polymer electrolyte membrane fuel cell Startup/shutdown Pt degradation Carbon corrosion Characterization

#### ABSTRACT

Despite the great progress that has been made in improving the performance of polymer electrolyte membrane fuel cells (PEMFCs), they still suffer from the degradation of catalyst components. Multiple startup/shutdowns (SUSDs) of a fuel cell electric vehicle (FCEV) is one of the situations in which the catalyst and its support degradation can cause PEMFC failure. Hence, in this study, comprehensive quantification of key microstructural parameters was implemented to correlate the microstructural changes with performance data of SUSD samples. Pt loss from the cathode and particle size distribution, as well as cathode porosity and thickness changes, were quantified and discussed with respect to the electrochemical performance. The reported values indicated severe carbon corrosion and Pt degradation during an unprotected SUSD operation at 35 °C. Moreover, the elevation of the operating temperature to 70 °C exacerbated the degradation to the point that the cathode catalyst layer collapsed after a low number of cycles. After a protective protocol was implemented, microstructural and electrochemical characterization showed a significant decrease in carbon corrosion and Pt degradation. The structure-property-performance relationship confirmed and quantified the effects of unprotected SUSD operation, but also showed how the protective protocol will preserve the microstructure of the PEMFC and hence improve its lifetime.

#### 1. Introduction

Fuel cells have been attracting attention in the past several decades as an enabler of clean energy generation. The ability to use a clean fuel such as hydrogen, in an emission-free energy electrochemical conversion process, with high efficiency and high power density, in addition to low operating temperature ( $<100~^{\circ}$ C) and a quick start-up, makes polymer electrolyte membrane fuel cell (PEMFC) an ideal candidate for commercial vehicles [1].

The structure of a common PEMFC consists of a number of components such as bipolar plates, gas flow field plates, gas diffusion layers (GDLs), and catalyst coated membranes (CCMs). The CCM, consisting of

a Center for Clean Energy Engineering, Institute of Materials Science, and Department of Materials Science and Engineering, University of Connecticut, 44 Weaver Rd. Unit 5233, Storrs, CT, 06269, USA

<sup>&</sup>lt;sup>b</sup> Ford Motor Company, 1 American Road, Michigan Avenue, Dearborn, MI, 48121, USA

<sup>\*</sup> Corresponding author.

E-mail address: jasna.jankovic@uconn.edu (J. Jankovic).

 $<sup>^{1}</sup>$  Deceased.

a proton-conductive solid polymer electrolyte membrane (PEM), sandwiched between the catalyst layers of the two electrodes - a cathode and an anode - is considered the heart of the fuel cell. All the electrochemical reactions happen in the CCM, namely the oxygen reduction reaction (ORR) at the cathode and the hydrogen oxidation reaction (HOR) at the anode, producing useful electrical current with water as a byproduct. At the same time, due to the harsh conditions during fuel cell operation, most of the degradation and performance loss also happens in the CCM, especially in the cathode. In addition, due to slow kinetics, the cathode reaction is the limiting factor for the performance of the PEMFC [2]. Platinum (Pt), as one of the best catalysts for ORR [3], has been widely used in PEMFCs, however, its high cost is considered one of the major challenges for these devices [1]. Therefore, the catalyst layer is designed in such a way as to minimize the amount of Pt used. The catalyst layer in the PEMFCs consists of Pt nanoparticles (2-5 nm in size) distributed on carbon support (consisted of 30-50 nm primary carbon particles and 100–300 nm carbon agglomerates), bound by a thin proton-conductive ionomer film (7–10 nm) to form a porous network [4,5] through which reactants and products of reactions are transported. While utilization of nanoparticles in the catalyst layer results in an increased surface area and improved catalyst activity [6], their stability decreases at the same time, attributed to the higher surface energy of nano-sized particles [7]. Hence, the degradation of the catalyst layer materials - i.e., Pt and carbon support - results in the loss of performance and durability of the PEMFC and hinders their mass adoption [8].

The degree and mechanisms of Pt and carbon degradation differ under different PEMFC operating conditions. One of the detrimental conditions that a PEMFC faces, when used in a fuel cell electric vehicle (FCEV), is startup/shutdown (SUSD). Detailed explanations available in the literature confirm that the formation of air/fuel boundary at the anode during the startup of the cell can cause a half-cell potential of above 1.4 V inside the cathode [9,10]. Such high potential of the cathode results in severe component degradation. While high potentials (E > 0.85 V under standard conditions) cause Pt dissolution/redeposition and transport of the Pt<sup>2+</sup> ions into the membrane [11], carbon corrosion is considered the most detrimental degradation mechanism under SUSD. Corrosion of catalyst support results in Pt agglomeration, loss of electrochemical surface area (ECSA) [8], electrode thinning, and, consequently, the collapse of the electrode [12]. Therefore, it is essential to implement carbon corrosion mitigation strategies to improve the durability of PEMFC utilized in FCEV. Yu et al. [13] reviewed the available mitigation strategies and reported that materials improvement and system mitigation are two effective approaches to reduce carbon corrosion and improve the durability of PEMFC. Improving the stability of the catalyst support through increasing the degree of carbon graphitization [14-16] or replacing the carbon with ceramic materials [17] showed that the material improvement strategy was effective. However, application of new materials inside the cathode can be challenging and costly. Therefore, system mitigation approaches can be more practical in preventing degradation. Purging the anode before startup and after shutdown, applying load to consume O<sub>2</sub> at the cathode, eliminating the high potential at the cathode by electrical short, and a combinations of the above approaches are proven as the best system mitigation processes

Although electrochemical characterization of PEMFC operated under SUSD with and without mitigation strategies is widely studied and reported in the literature [12,18], the analysis of the microstructure of the electrode layers, both "as built" and after SUSD degradation, needs further attention. Understanding the structure-property-performance relationships for PEMFCs, in general, has often been the focus of research groups. As evidenced in reports from the U.S. Department of Energy, understanding the microstructure of PEMFC and correlating it to the performance and durability has been recognized as crucial to support PEMFC development and wide adoption [19]. Available literature shows a wide variety of studies, from modeling to experimental approaches, focusing on the significance of the microstructure in different

components of the PEMFC - GDLs [20,21], catalyst and its support [22-28], catalyst inks [29,30], catalyst layers [19,27,28,31,32], and membrane/ionomer phase [33,34]. Moreover, it is believed that observing the changes by microscopy techniques can unravel the details about the components' degradation and the mechanism of degradation [11,23,25,28,35–42]. An especially important aspect of microstructural characterization is quantification of structural and compositional parameters, and their correlation to performance and degradation. Above mentioned studies reported a number of quantified parameters, ranging from catalyst layer thickness, crack density and length, catalyst particle size distribution, pore size distribution, overall CCM Pt loading (Pt amount in cathode, membrane and anode was not possible to distinguish), etc., using various techniques. However, other key microstructural and compositional parameters, such as quantified changes of Pt loading in the cathode and loss to the membrane, electrode primary and secondary porosity, and ionomer to carbon weight ratio (I/C), together with other structural parameters, especially in the end-of-life (EOL) electrodes, have been challenging to determine. Our team has developed a quantification approach to address this challenge using a single technique, with both visualization and quantification obtainable for the same areas, in both beginning-of-life (BOL) and EOL samples [30, 43-45]. Therefore, in the current study, a comprehensive microstructural characterization and parameter quantification was performed to evaluate and quantify the effects of degradation for membrane electrode assemblies (MEAs) that were exposed to unprotected system-protected SUSD protocols. The microstructural analyses were studied with respect to the electrochemical characterization to better understand the performance and durability changes under different SUSD protocols. The approach offers a unique capability to quantify these values in both BOL and EOL electrodes, revealing structure-performance correlations, and an opportunity to understand the main factors that contribute to the MEA failure.

# 2. Experimental procedure

## 2.1. Materials

Commercial CCMs with cathode and anode catalyst loadings of 0.25  $\rm mg_{Pt} cm^{-2}$  and 0.05  $\rm mg_{Pt} cm^{-2}$ , respectively, were used to fabricate the MEAs. PtCo and Pt on high-surface-area carbon support were the catalysts for the cathode and the anode, respectively. A reinforced perfluorosulfonic acid (PFSA) polymer electrolyte membrane (PEM) with a thickness of  $\sim\!15~\mu m$  was used. Two SGL 29BCE gas diffusion layers were used on the cathode and the anode to sandwich the as-received CCM. These MEAs were fabricated by hot compression at 160 °C, 1400 lb for 150 s. The untested MEA did not undergo any pre-treatment and was used as the BOL sample. A Core Attribute Testing (CAT) cell with an active surface area of 40 cm² and straight flow channels (channel dimensions 112.5 mm L  $\times$  0.25 mm W  $\times$  0.4 mm D on the cathode plate and 0.24 mm D on the anode plate) was used for testing.

#### 2.2. Testing and diagnostics procedures

BOL conditioning was carried out for 12 h under 1.2 A cm $^{-2}$  at 60 °C while the relative humidity (RH) was kept at 100%. ECSA, polarization at 1.2 A cm $^{-2}$  (mass transport region) and 0.02 A cm $^{-2}$  (kinetics region), and high frequency resistance (HFR) were measured at BOL, after every 500 cycles, and at EOL. ECSA measurements were conducted by averaging the hydrogen adsorption and desorption charges considering 210  $\mu C \ cm_{Pt}^{-2}$  as the desorption charge of one monolayer of hydrogen from Pt. The adsorption and desorption charges were extracted from cyclic voltammetry (CV) (acquired by Zahner IM6 potentiostat) of the cathode, performed at a scan rate of 20 mV s $^{-1}$  and in the potential range of 0.05–0.6 V vs. the dynamic hydrogen electrode (DHE) (the anode was both the counter and the reference electrode). During CV evaluation, the cathode temperature and RH were kept at 80 °C and 100%, respectively,

while 4 SLPM  $\rm H_2$  and 8 SLPM  $\rm N_2$  were purged through the anode and cathode, respectively. The procedure for ECSA measurement is explained in the previous work [46]. Polarization measurements were conducted at 80 °C and 100% RH when 1 SLMP  $\rm H_2$  and 2 SLPM air were purged on the anode and the cathode, respectively, keeping the pressure on both sides at 150 KPa. The voltages reported here are the average cell voltages in the last minute of hold at the respective current density. HFR was measured by applying a constant load of 1.2 A cm<sup>-2</sup> for 30 min in the range of 100 mHz-100 kHz with an amplitude of 10 mV. Diagnostics were performed every 500 cycles. A cell voltage below 0.1 V at 1.2 A cm<sup>-2</sup> was considered the failure criterion for the cell. Recovery protocol from US DRIVE Fuel Cell Tech Team was applied before diagnostics to recover reversible losses [47]. The final target of 5000 cycles was the total run time of the cell. Detailed procedure and diagnostic results at every 500 cycles are presented in previous work [46].

#### 2.3. SUSD procedure

Schematic representations of SUSD protocols are presented in previous work [46] and Fig. 1.

Unprotected SUSD: The accelerated stress test (AST) SUSD, simulating an unprotected shutdown was carried out on the MEAs. In the first step of the AST, the PEMFC was operated normally for 60 s under load. The next step involved a shutdown by shutting off the gas supplies and eliminating the load, creating an OCV condition for 10 s (due to remaining gases in the electrodes). After that, the air was introduced into the system and the cell underwent a soak process by purging air through the anode and cathode for 60 s, with the cell voltage falling to zero. Following that, the air was stopped on the anode (while still flowing air on the cathode) and  $H_2$  was introduced to the anode during the startup for 10 s. The voltage reached OCV values. The OCV conditions and the air/fuel boundary in the anode are expected to cause

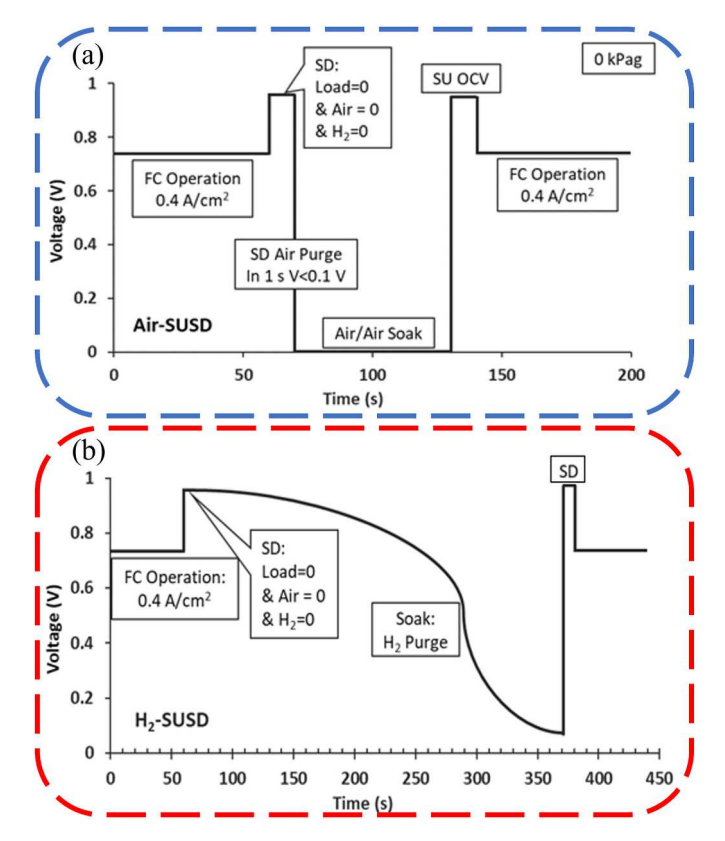


Fig. 1. Schematic representations of (a) Air-SUSD and (b)  $H_2$ -SUSD. A full cycle consisted of an operation at 0.4 A cm<sup>-2</sup>, shutdown, soak, and a startup. Reproduced from Ref. [46].

carbon corrosion in the cathode [10]. The next step involved the normal cell operation at 0.4 A cm $^{-2}$  that lasted for 60 s (Fig. 1a). The unprotected AST SUSD operation step was conducted on two MEAs at 35 °C (Air-SUSD-35 °C) and 70 °C (Air-SUSD-70 °C) [46].

Hydrogen protection protocol was applied to the third MEA ( $\rm H_{2}$ -SUSD-35 °C): The protocol was intended to provide carbon protection during the transition between the shutdown and the startup phase. While the PEMFC operation remained the same, the shutdown started with closing the gases and unloading the cell in a 10 s process. Here,  $\rm H_{2}$  was introduced again to the anode while no air was supplied to the cathode. By this means,  $\rm H_{2}$  permeation from the anode to the cathode created a  $\rm H_{2}$  soak condition in the cathode to consume  $\rm O_{2}$  inside the cathode. Also, in this way, the air was not introduced to the anode, preventing air/fuel boundary and carbon corrosion. As the process is a permeation one, 300 s were given to the cell and then, the startup was initiated (Fig. 1b) [46].

### 2.4. Microstructural analysis

SEM, TEM, and STEM-EDS: Scanning Electron Microscopy (SEM) sample preparation started by embedding a 2 cm  $\times$  1 cm sections of the MEAs in EpoThin epoxy resin (BUEHLER, USA). The sections were polished in an automated polishing machine (Struers LaboPro-5, Denmark), using 60-, 240-, 600-, and 1200-mesh grinding papers, followed by polishing the samples with 5 µm diamond and then 0.1 µm alumina polishing paste (BUEHLER, USA), and then coated with a few nanometers of gold (Denton Vacuum LLC, USA). The cross-sectional SEM imaging of the MEAs was completed with a Teneo LV SEM (Thermo Fisher Scientific, USA) at 1000× and 5000× magnification using a circumferential backscattered (CBS) detector. The open-source Fiji ImageJ software was used to measure the thickness of the cathodes, membranes, and anodes. The thicknesses reported here are the average of measurements in at least 7 different regions of the MEAs, for each of which the measurement was repeated in at least 10 different locations.

Next, a tweezer was used to peel off the GDL from each MEA, and then a 1 cm  $\times$  0.5 cm section of the bare CCMs were cut with scissors for transmission electron microscopy (TEM) sample preparation. A small piece of each CCM was embedded in a 1:1 mixture of resin (Sigma-Aldrich, USA) and hardener (Sigma-Aldrich, USA) and polymerized overnight to prepare the sample for the ultramicrotomy. Thin sections (approximately 100 nm thick) were cut by Leica UCT ultramicrotome setup (Germany) equipped with an Ultra 45° DiATOME knife, USA. The sections were mounted on multiple 200 mesh Cu/Pd grids. A Talos F200X STEM (Thermo Fisher Scientific, USA) equipped with Super-X four silicon drift detectors of energy dispersive X-ray spectrometry (Super-X SDD EDXS, Bruker, USA) at a solid angle of 0.9 steradian with electron accelerating voltage of 200 kV was utilized for imaging and elemental mapping of the samples. The TEM images at 190kx of at least 5 different randomly selected regions were acquired by the bright field detector (BF-TEM) and the size of a total number of 200 platinum particles was measured by Fiji ImageJ to extract the particle size distribution (PSD). The scanning transmission electron microscopy with energy dispersive spectroscopy (STEM-EDS) mapping was done at 5 kx magnification. The EDS maps were acquired with an electron dose of  $2.34 \times 10^4 \, \mathrm{e^-} \, \mathrm{nm}^{-2}$ . Further elemental analysis and raw data extraction were carried out by the ESPIRIT 1.9 (Bruker, USA) analytical software.

Microstructural descriptors quantification: The collected STEM-EDS elemental maps data was used in a previously developed quantification method to determine the electrode primary porosity (assumed to be within Pt/C agglomerates with d < 5 nm [48]), secondary porosity (assumed to be between Pt/C agglomerates with d > 5 nm [48]) and total porosity, as well as Pt loading. The method is based on a modified  $\zeta$ -factor approach [49], in which the amount of an element (mass, concentration, or thickness) in an analyzed region is determined based on the measured intensity of its X-ray signal. The  $\zeta$ -factor approach

states that in a thin-film specimen (like the CCM sections on the TEM grid), the measured element's characteristic X-ray intensity,  $I_A$ , is proportional to the  $\rho$  (mass)  $\times$  t (thickness), and the concentration,  $C_A$ . A detailed description of the technique is published in the previously reported work [43,46,50]. The reported values are the average of measurements and quantification of at least three randomly selected and analyzed regions (of approximately  $10~\mu m \times 10~\mu m$  size). It should be noted that the Pt loading values reported by quantification of the BOL samples have acceptable agreement (within 5%) with the information provided by the vendor. The methodologies have been previously used on different MEAs and showed a high degree of reliability [30,43,44,46].

#### 3. Results and discussions

The results of the performance and diagnostics for the tested MEAs under different SUSD protocol are shown in Table 1 and Fig. 2.

A comprehensive analysis of all microstructural effects was done using both conventional image analysis methods (e.g., SEM catalyst layer thickness and TEM Pt PSD), as well as the above-mentioned quantification approach (for BOL and EOL porosity measurements, Pt loss, and Pt/Co atomic ratio using STEM-EDS elemental map data [30, 43]). To the authors' knowledge, this level of comprehensive characterization and microstructural analysis with quantification has not been previously reported by other researchers. In this work, the method is applied to the BOL and all EOL samples after the SUSD operation.

SEM characterization and quantification. SEM images (Fig. 3c and d) show two major effects in the unprotected SUSD sample when compared to the BOL (baseline) sample (Fig. 3a and b): cathode thinning and deposition of Pt particles in the membrane in a form of a Pt-rich band. Air-SUSD-35 °C operation without any protective protocol resulted in the air/fuel boundary formation in the anode, and a spike in the cathode voltage [10,51], causing cathode carbon corrosion and a 29% reduction in the cathode thickness (Table 2). The thinning of the cathode was mainly attributed to the loss of carbon support through carbon corrosion [52]. In addition, the formation of a Pt-rich band in the membrane close to the cathode, and at the interface of the anode/membrane indicated a large amount of Pt loss from the cathode (quantified to be 50%, as discussed later), which was a consequence of the harsh environment of SUSD operation (e.g., Pt dissolution/redeposition in the membrane due to high potentials and concentration gradients [9]). A large loss in the

Table 1
Diagnostic results of three tested MEAs under different SUSD protocols [46].

Sample	Cycle Number	Cell Voltage at 0.02 A cm <sup>-2</sup> (mV)	Cell Voltage at 1.2 A cm <sup>-2</sup> (mV)	ECSA <sub>ave</sub> $(m^2/g_{Pt})$
Air-SUSD-	0	911	650	10.59
<b>70</b> °C	500	875	618	10.24
	100	817	63	4.94
Air-SUSD-	0	906	620	12.65
35°C	455	896	630	12.06
	910	878	594	9.06
	1365	864	512	7.51
	1820	854	402	6.64
	2275	845	306	5.64
	2730	848	86	4.64
H <sub>2</sub> -SUSD-	0	903	655	12.23
<b>70</b> °C	500	908	646	15.04
	1000	906	656	15.14
	1500	903	635	14.46
	2000	894	622	14.70
	2500	898	618	14.96
	3000	911	617	13.23
	3500	913	598	14.76
	4000	912	594	13.71
	4500	907	591	13.64
	5000	900	590	14.01

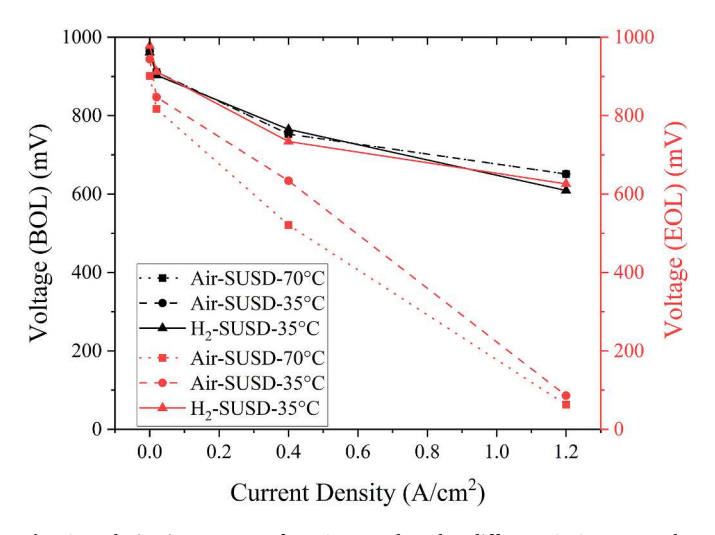


**Fig. 2.** Polarization curves of MEAs tested under different SUSD protocols. Black lines represent BOL performances (note: Air-SUSD-35  $^{\circ}$ C and Air-SUSD-70  $^{\circ}$ C overlap), while red lines show the EOL results. (For interpretation of the references to colour in this figure legend, the reader is referred to the Web version of this article.)

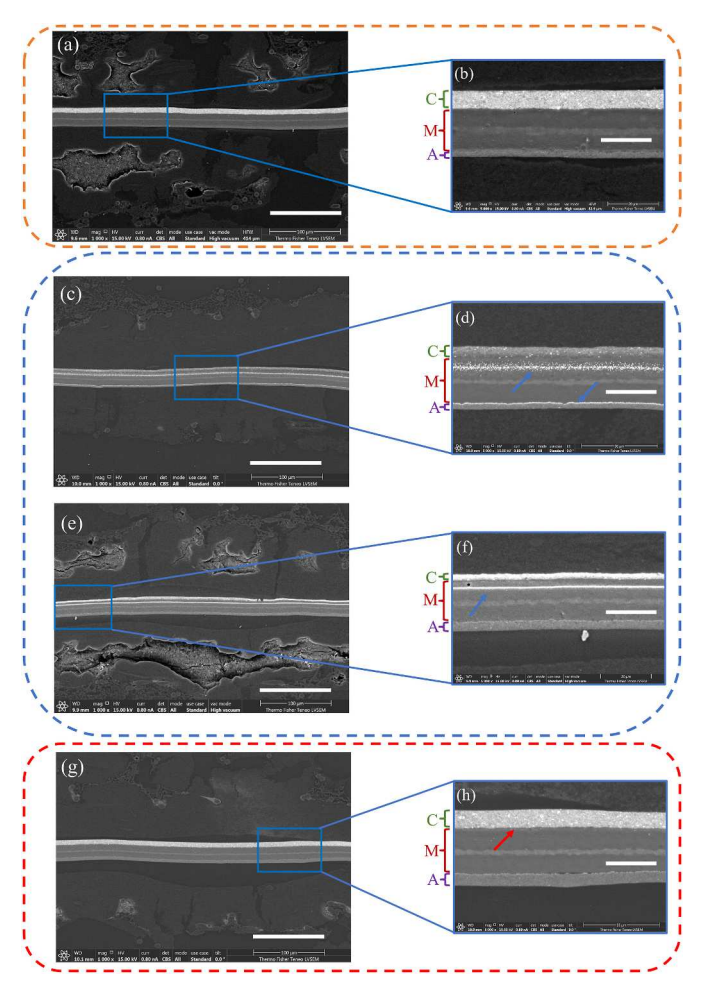


Fig. 3. SEM cross-section images of (a) BOL at 1000 x, (b) BOL at 5000 x, (c) Air-SUSD-35 °C at 1000 x, (d) Air-SUSD-35 °C at 5000 x, (e) Air-SUSD-70 °C at 1000 x, (f) Air-SUSD-70 °C at 5000 x (g)  $\rm H_2\text{-}SUSD\text{-}35$  °C at 1000 x, and (h)  $\rm H_2\text{-}SUSD\text{-}35$  °C at 5000 x. The CCMs are sandwiched between two GDLs of which fibers and MPL layer are observable at 1000 x. The scale bars on 1000 x images and 5000 x are 100  $\mu m$  and 20  $\mu m$ , respectively.

**Table 2**Comparison of layer thicknesses of BOL and SUSD samples.

Sample	Cathode (µm)	Membrane (μm)	Anode (µm)
BOL	$\textbf{7.4} \pm \textbf{0.4}$	$17.0 \pm 0.5$	$3.5 \pm 0.4$
Air-SUSD-35 °C	$5.2 \pm 0.2  (-29\%)$	$17.7\pm0.3$	$3.9 \pm 0.3$
Air-SUSD-70 °C	$3.4 \pm 1.1 \; (-54\%)$	$16.6\pm0.6$	$3.6 \pm 0.8$
H2-SUSD-35 °C	$6.7 \pm 0.2 \ (-8\%)$	$17.4\pm0.4$	$4.1\pm0.2$

ECSA ( $\sim$ 63% (Table 1)) and performance (cell potential in Table 1 and Fig. 2) confirmed the loss of active surface area of the catalyst [46] to the point that the cell failed before completing 3000 cycles. However, as discussed below, ECSA loss was not the only cause of the failure.

To study the effect of temperature on Pt degradation, carbon corrosion, and cathode microstructure, the Air-SUSD test was repeated under the cell temperature of 70 °C (per the procedure explained in the experimental section and the previous work [46]). It should be noted that Air-SUSD-70 °C sample failed at 1000 cycles [46], with the ECSA loss of 53% (Table 1). The lower ECSA loss for Air-SUSD-70 °C MEA that failed much earlier, compared to Air-SUSD-35 °C indicates that other factors contributed to the failure, such as carbon corrosion and loss of porosity, as discussed below and later. Indeed, SEM cross-section comparison of the samples tested at two different temperatures (Fig. 3c and d compared to Fig. 3e and f) showed distinct differences between Air--SUSD-35 °C compared to Air-SUSD-70 °C in reference to the BOL sample. The first feature is a brighter contrast of the cathode in the Air-SUSD-70 °C sample. The higher temperature will accelerate the kinetics of carbon corrosion in the cathode [53]. The result of the thickness measurements (Table 2) was affirmative of this expectation with 54% thinning of the cathode in Air-SUSD-70 °C compared to a 29% thinning of the Air-SUSD-35 °C sample. Consequently, a higher rate of carbon corrosion resulted in a more compact cathode, with higher contrast in CBS-SEM images. More aggressive degradation conditions also caused a denser Pt-rich band in Air-SUSD-70  $^{\circ}\text{C}$  (with a quantified Pt loss from the cathode of 60%, as discussed later), compared to Air-SUSD-35 °C (50% Pt loss). It is interesting to note that Air-SUSD-70 °C sample had a lower ECSA loss (53%), even though its cathode lost more Pt to the membrane (60%), compared to Air-SUSD-35 °C (ECSA loss of 63%, with a Pt loss of 50%). The other feature is a lack of Pt band at the interface of anode/membrane in Air-SUSD-70 °C due to a lack of permeation of Pt<sup>2+</sup> ions to the anode and redeposition at the interface. This could be due to a higher diffusion rate of Pt<sup>2+</sup> ions and a higher permeation rate of H<sub>2</sub> inside the membrane [54] (Fick's law) at a higher temperature. A higher operation temperature increased the H<sub>2</sub> crossover exponentially [55], preventing more transport of Pt2+ ions toward the anode and formation of the Pt-rich band inside the membrane at its specified location [11,37]. This needs to be studied further to understand the effect of the H2 flow rate and its permeation under different SUSD operation conditions.

As expected, the  $\rm H_2$ -soak of the anode in  $\rm H_2$ -SUSD-35 °C operation (protected) created a protective condition by preventing air/fuel boundary formation and avoiding high local potential in the cathode ( $\sim$ 1.5 V). As a result, the cathode thinning was only 8% (Table 2 and Fig. 3g, h) while the formed Pt band in the membrane was not as rich in Pt (quantified Pt loss from the cathode was only 10%) as in the unprotected samples. In this case, the cell could complete all 5000 cycles [46] with acceptable performance and no ECSA loss (Table 1 and Fig. 2). This is an indication of the effect of the protective protocol on the improvement of the cell lifetime under the SUSD operation.

The discussion from the SEM characterization in this section indicated that the performance and the ECSA losses, as well as MEA failures are related to the Pt loss from the cathode and electrode thinning caused by carbon corrosion. However, further analysis by STEM-EDS and quantification of additional parameters, discussed next, will provide more clarity on the degradation effects.

STEM-EDS analysis and quantification. As previously reported [45,

46,56], Pt degradation through different mechanisms was expected in the SUSD samples. Therefore, it is essential to have the PSD analysis of the cathode Pt catalyst particles to study the possible predominant Pt degradation mechanism during the SUSD operations [35]. For this purpose, PSD analysis of Pt particles, as per the TEM procedure explained in the experimental section, was performed on the BOL and EOL samples. Table 3 shows the mean particle size of Pt particles in the cathode of BOL and SUSD samples. The Pt mean particle size increased 13% for Air-SUSD-35 °C and 22% for Air-SUSD-70 °C, which was indicative of Pt degradation and ECSA loss. To understand the predominant mechanism for ECSA loss, the PSD histograms of all SUSD samples, compared to BOL, along with the TEM images at 190 kx are presented in Fig. 4. As shown in Fig. 4b and Fig. 4c, both Air-SUSD samples have a wider histogram indicating the presence of the Ostwald ripening degradation mechanism [35]. Moreover, both histograms of Air-SUSD-35 °C and Air-SUSD-70 °C have a tail toward bigger particles showing the presence of agglomeration of the particles [11,36]. Therefore, it could be concluded that Pt dissolution/redeposition, Ostwald ripening, and particle agglomeration due to carbon corrosion and Pt detachment were all active during the degradation of the cathode catalyst layer. However, the widening of the histogram for the Air-SUSD-70 °C sample was more prominent than that of Air-SUSD-35 °C, denoting a more severe Pt agglomeration due to loss of catalyst support and formation of isolated and agglomerated Pt particles. Finally, the change in the mean particle size of the protected H<sub>2</sub>-SUSD-35 °C MEA was negligible, compared to the BOL MEA (Table 3). Its PSD histogram in Fig. 4 d shows a widening, while the tail is negligible. Therefore, Ostwald ripening of Pt particles could be considered the predominant Pt degradation mechanism in this case. However, no changes in the Pt mean particle size and small changes in the PSD confirmed that the protective protocol was effective in preventing degradation.

Further detailed microstructural analyses require STEM-EDS and quantification studies. Low-magnification high-angle annular dark-field scanning transmission electron microscopy (HAADF-STEM) images and STEM-EDS elemental distribution and intensity maps of Pt are shown in Fig. 5. Fig. 5b and c shows a uniform distribution of Pt inside the BOL cathode catalyst layer, without any Pt presence inside the membrane (below the interface of the membrane and the cathode labeled by an orange line in the image). The STEM-EDS distribution map of Pt for Air-SUSD-35 °C in Fig. 5 e shows a Pt depletion zone in the cathode at the cathode/membrane interface (blue line), with a Pt concentration gradient decreasing from GDL side toward the membrane. In addition, a heavy Pt-rich band is present inside the membrane showing Pt degradation inside the cathode by Pt dissolution/redeposition mechanism [11]. The STEM-EDS elemental distribution intensity map of Pt in Fig. 5 f confirms both the Pt gradient formation inside the cathode and the Pt-rich band presence inside the membrane. Fig. 5 h shows the Pt distribution in the cathode catalyst layer of Air-SUSD-70 °C with a thick Pt-rich band inside the membrane. Unlike the EDS elemental distribution intensity map of Pt in the Air-SUSD-35 °C cathode catalyst layer, the Pt intensity map of the cathode of Air-SUSD-70 °C (Fig. 5i) does not show a severe Pt gradient. The observation could be related to the effect of temperature on the diffusion rate and concentration of  $\operatorname{Pt}^{2+}$  ions inside the cathode, the thickness of the catalyst layer, and the changes they can cause in the Pt loss rate governed by Fick's first law [57]; the fact needs more in-depth study. On the other hand, the H2-SUSD-35 °C

**Table 3**PSD analysis of BOL and SUSD samples.

Sample	Mean particle size (nm)
BOL	$6.40\pm2.7$
Air-SUSD-35 °C	$7.25\pm3.54$
Air-SUSD-70 °C	$7.78 \pm 5.16$
H2-SUSD-35 °C	$6.03 \pm 4.48$

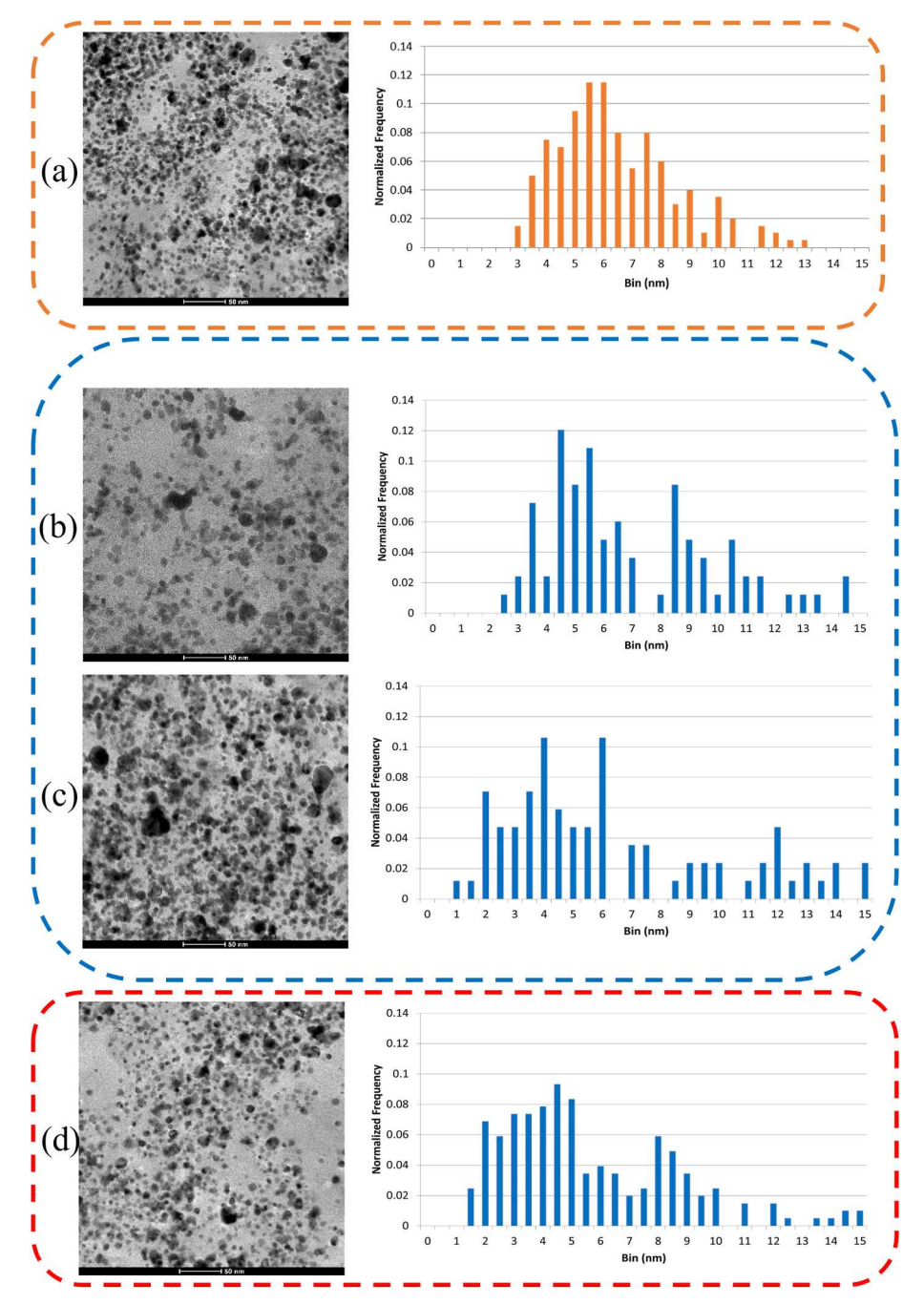


Fig. 4. BF-TEM image and PSD analysis histogram of (a) BOL, (b) Air-SUSD-35 °C, (c) Air-SUSD-70 °C, and (d) H<sub>2</sub>-SUSD-35 °C.

sample STEM-EDS Pt elemental distribution and intensity maps (Fig. 5h and i), show a uniform, gradient-free, distribution of Pt like that of the BOL (Fig. 5b and c). Dispersed Pt particles can be intermittently seen inside the membrane and in the vicinity of the cathode/membrane interface (blue line). The visual Pt map results, together with the PSD analysis, confirmed that the Pt dissolution/redeposition mechanism caused Pt degradation during the protected SUSD operation, the intensity and rate of which was lower than that of unprotected (Air-SUSD-35 °C and Air-SUSD-70 °C) operations.

Table 4 presents all microstructural and compositional parameters derived from STEM-EDS quantification for BOL and SUSD samples. Table 4 is arranged in such a way that it represents the results starting from the BOL (no degradation), then the minimally degraded  $\rm H_2\text{-}SUSD-35~^{\circ}C$  sample, followed by moderately degraded Air-SUSD-35  $^{\circ}C$  sample, and finally severely degraded Air-SUSD-70  $^{\circ}C$ .

Pt loading in the cathodes of the samples was quantified using a method reported in Ref. [43]. Air-SUSD-70 °C showed a severe Pt loading loss of 60% from the cathode and the formation of a spatially concentrated Pt-rich band in the membrane. Air-SUSD-35 °C lost 50% of Pt loading while H<sub>2</sub>-SUSD-35 °C showed a minimal Pt loading loss of 10% with an intermittent presence of Pt particles inside the membrane close to the cathode/membrane interface. Pt/Co atomic ratio in the cathodes also had a trend in agreement with the degradation severity: Air-SUSD-70 °C sample showed a severe loss of both Pt and Co into the membrane, with a higher rate of Co leaching, while Air-SUSD-35 °C Pt sample showed less Co loss and the Pt/Co ratio stayed close to that of the BOL. H<sub>2</sub>-SUSD-35 °C showed an increase of Pt/Co atomic ratio in the cathode, indicating a low rate of Pt loss with a higher rate of Co leaching out of the catalyst layer [58].

The Pt loading change versus the operation condition of each sample

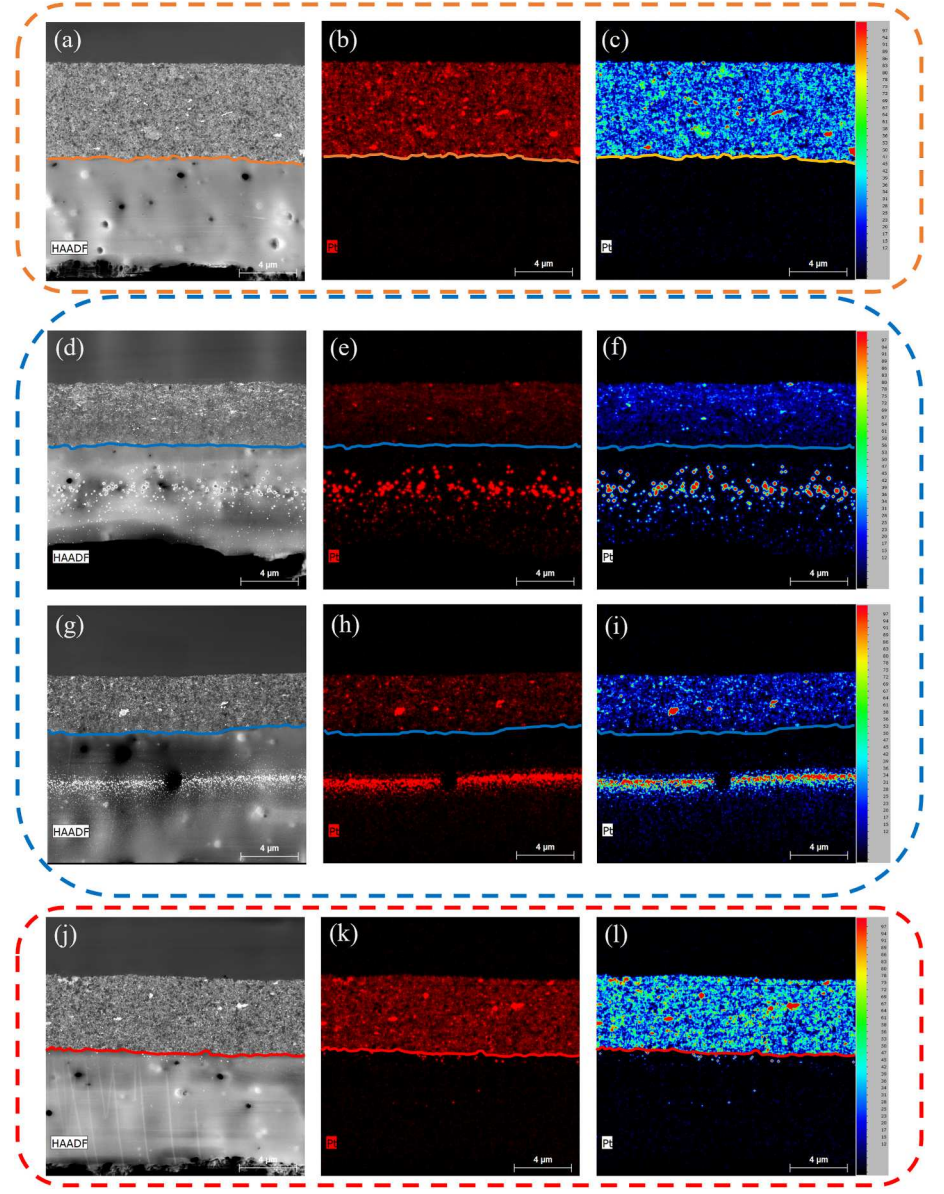


Fig. 5. BOL (a) HAADF image, (b) EDS elemental distribution map of Pt, (c) EDS elemental distribution intensity map of Pt. Air-SUSD-35 °C (d) HAADF image, (e) EDS elemental distribution map of Pt, and (f) EDS elemental distribution intensity map of Pt. Air-SUSD-70 °C (g) HAADF image, (h) EDS elemental distribution map of Pt, and (i) EDS elemental distribution intensity map of Pt. H<sub>2</sub>-SUSD-35 °C (j) HAADF image, (k) EDS elemental distribution map of Pt, and (l) EDS elemental distribution map of Pt at 5 kx.

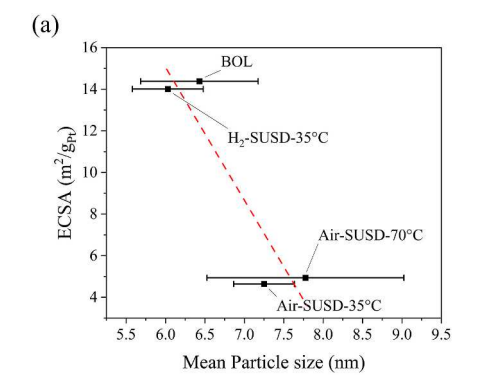
is presented in Fig. S1. The trends of Pt loading changes were in agreement with the expectations that the unprotected cathodes have more Pt degradation and loss. However, although the severity of degradation in the cathode of Air-SUSD-70 °C, after an early failure at 1000 cycles, was higher than that of Air-SUSD-35 °C, the Pt loading difference in those samples was minimal. This points out, as discussed earlier, to other factors contributing to the failure, including but not limited to the severe thinning of the cathode of Air-SUSD-70 °C, the drop of chemical potential as the Pt concentration declines inside the cathode [59], and loss of electrical conductivity and porosity of the cathode due to carbon corrosion [53].

To understand the structure-performance relationship, the ECSA of the cathode was plotted versus mean particle size and Pt loading. As reported previously, ECSA is directly proportional to Pt particle size and Pt loading. A decrease in ECSA with an increase in mean particle size and a decrease in Pt loading was expected from the samples [3]. The relationship between ECSA of SUSD and BOL samples with mean particle size (Fig. 6a) and Pt loading (Fig. 6b) showed reasonably good R-squared (R²) values of 86% and 97%, respectively. It should be noted that the ECSA value considered here are the data from EOL (either failure point or end of 5000 cycles).

According to the analyses performed here and reports in the literature, experiencing a potential of  $\sim 1.5$  V in the cathode during the startup can result in severe carbon corrosion and Pt degradation. It is expected to see an electrochemical dissolution and oxidation of Pt, transport of Pt<sup>2+</sup> ions in the cathode and toward the anode, and detachment of Pt particles (at a higher rate compared to migration) from the support. Carbon corrosion can enhance the migration and/or detachment of Pt particles and the formation of isolated Pt aggregates/ agglomerates. During unprotected startup, the Pt dissolution and migration/detachment from the corroded support resulted in the formation of Pt2+ ions and aggregation of Pt particles, respectively. A fraction of Pt<sup>2+</sup> ions were transported and redistributed throughout the cathode, while other Pt<sup>2+</sup> ions were carried away from the cathode and transported into the membrane and toward the anode (mostly during normal operation). After SU, the normal operation of the cell proceeded and resulted in the reduction and redeposition of the  $\operatorname{Pt}^{2+}$  ions inside the cathode through either crossed-over H2 or electrochemical reduction. The consequence of this a process was seen in the mean particle size growth, PSD histogram changes, and ECSA loss. Consequently, the performance and durability losses were observed as expected. The Pt<sup>2+</sup> ions inside the membrane met crossover H2 and the reduction to form a

**Table 4**The cathode microstructural parameters quantification results for the BOL and the SUSD samples.

Descriptor	Sample			
	BOL	$H_2$ SUSD-35 $^{\circ}$ C	Air SUSD-35 °C	Air SUSD-70 °C
Primary porosity (%)	$45\pm3$	$41\pm 8$	$37\pm3$	$39 \pm 4$
Secondary porosity (%)	$26\pm3$	$32 \pm 9$	$26\pm2$	$34\pm3$
Total porosity (%)	$71\pm3$	$73\pm3$	$63 \pm 3$	$73\pm0$
Volume of primary porosity normalized to slice thickness $\times 10^{-7}$ (cm <sup>3</sup> /cm	$5.42 \pm 0.38$	$5.23\pm0.51$	$4.51\pm0.68$	$2.55\pm0.34$
Volume of secondary porosity normalized to slice thickness $\times$ 10 <sup>-7</sup> (cm <sup>3</sup> /cm)	$3.15\pm0.27$	$3.92\pm0.2$	$2.89 \pm 0.27$	$2.15\pm0.14$
Volume of CL total porosity normalized to slice thickness $\times 10^{-7}$ (cm <sup>3</sup> /cm)	$8.57\pm0.31$	$9.15\pm0.28$	$7.4\pm0.95$	$4.7\pm0.22$
Pt loading (mg <sub>Pt</sub> /cm <sup>2</sup> )	$0.20\pm0.02$	$0.18\pm0.03$	$0.10\pm0.01$	$0.08 \pm 0.01$
Pt/Co atomic ratio	$3.29\pm0.30$	$4.84\pm0.08$	$3.73\pm0.12$	$5.36 \pm 0.12$
Local cathode thickness (µm)	$6.7\pm0.1$	$6.8 \pm 0.5$	$6.3\pm1.0$	$3.6 \pm 0.2$



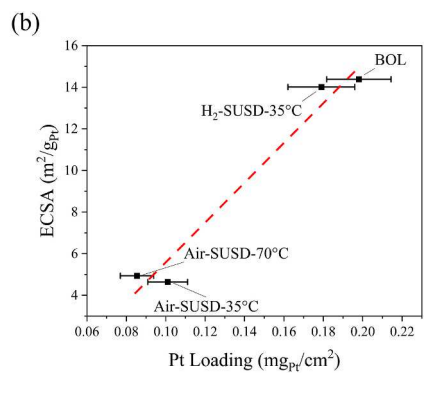


Fig. 6. The relationship of (a) ECSA and mean particle size and (b) ECSA and Pt loading for SUSD and BOL samples.

Pt-rich band inside the membrane was completed.

Further study involved an investigation of the effects of SUSD protocols on the porosity of the cathode layer. All three types of porosities – i.e., primary, secondary, and total – were determined using the microstructural parameter quantification method reported in Ref. [30]. The volumes of all porosity values were normalized to the ultramicrotomed slice thickness for each sample to eliminate the effect of possible sample preparation differences in the comparison of the changes.

Fig. 7 compares the volume of three types of porosities for all samples. The H<sub>2</sub>-SUSD-35 °C sample did not show a significant change in porosity compared to BOL. However, the wide standard deviation (SD) of the secondary porosity for H2-SUSD-35 °C pointed out the nonuniformity of degradation (as expected for the cathodes with a similar Pt loading as the one in this study [60]). Air-SUSD-35 °C showed a decrease in all three porosities, compared to BOL. The loss of porosity was assigned to carbon corrosion. A higher rate of carbon corrosion caused a loss of mechanical integrity of the cathode, due to the loss of carbon mechanical strength, and resulted in a drop in all three types of porosities. As testing conditions became more aggressive in Air-SUSD-70 °C, carbon corrosion resulted in a more extreme degradation of the microstructure. Loss of mechanical integrity of the layer resulted in the compression of the layer and reduced primary, secondary, and total porosities. The results were in line with SEM cross-section images and thickness measurements, where the severity of carbon corrosion caused the collapse of the cathode catalyst layer.

The effect of the porosity on the cell performance was studied further. Two cell voltages, in the kinetics region, at 0.02 A cm<sup>-2</sup>, and in the mass transport region, at 1.2 A cm<sup>-2</sup>, were used to study the relationship between the voltage in different current regions and the total cathode pore volume. The voltage in the kinetic region showed a good relationship with total pore volume with an R-squared of 85% (Fig. 8a) while the mass transport showed less dependence on the total catalyst layer volume of porosity with an R-squared of 67% (Fig. 8b).

That observation was against the expectations that the higher pore volume could help mass transport and improve the cell voltage at high loads. However, it should be noted that the correlation of cell voltage in kinetics- and mass transport-limited regions is a function of several factors including the porosities, Pt utilization, and diffusion pathway of reactants/product [3]. As reported by Marie et al. [61], the penetration of ionomer into the pores during the operation can also affect the voltage responses of the cell. Therefore, the correlation of the cell voltage to microstructural descriptors needs a more detailed study of the behavior of each element of the MEAs, especially the ionomer. A reliable imaging technique, as reported [62], needs to be implemented on the samples to understand the role of ionomer in the performance and durability degradation of the cell.

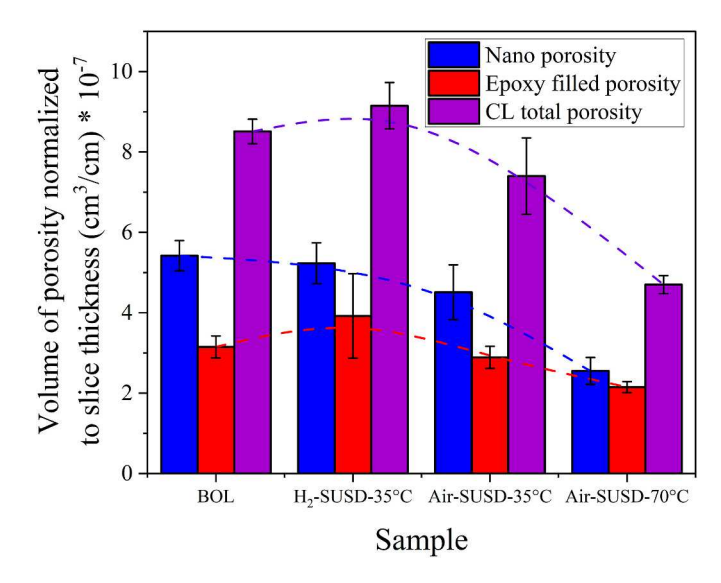
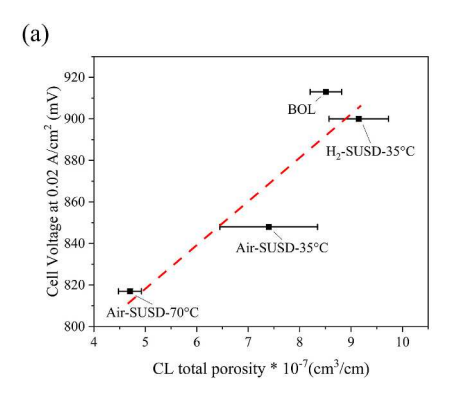


Fig. 7. Comparison of the volume of three types of porosities for SUSD and BOL samples.



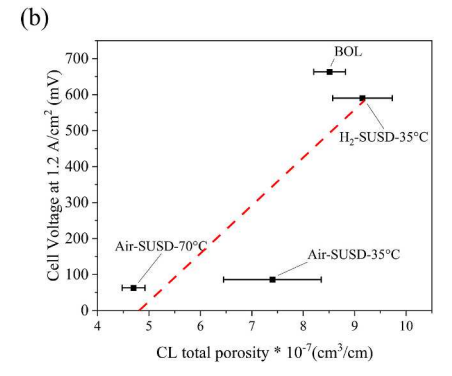


Fig. 8. The relationship between (a) voltage in the kinetic region and cathode total pore volume; (b) voltage in the mass transport region and the cathode total pore volume for SUSD and BOL samples.

#### 4. Conclusion

In this study, a comprehensive microscopy characterization and quantification approach was implemented to investigate the effect of unprotected SUSD operation at two different temperatures in addition to protected SUSD on a commercial CCM. The microstructural and performance analysis showed that the formation of an air/fuel boundary in an unprotected SUSD can cause the failure of the cell prior to 3000 cycles due to carbon corrosion, loss of porosity, Pt degradation and decrease of the Pt loading in the cathode. An increase in temperature in such an operation worsened the conditions to the point that the cell failed at 1000 cycles, the cathode catalyst layer collapsed, porosity dropped drastically, and the Pt loading decreased by 60%. The utilization of a protective protocol through a hydrogen soak of the anode during shutdown decreased the degree of Pt degradation and carbon corrosion, and the cell completed the 5000 cycles. The microstructural analysis showed a minimal change in the microstructure of the cathode in the cell operated under the protective protocol. It can be concluded from the microstructure and performance data relationships in this study, that microstructural changes caused by degradation in a PEMFC are directly related to cell performance. Even though this is expected, the quantification of the changes could help determine the relative effects of different operation procedures, as well as the relative effects of each of the microstructural parameters. The current report showed the feasibility of relating the electrochemical and microstructural characterization results, even for the severely degraded samples, in which quantification of microstructure can be challenging. This approach is a useful tool for the research and manufacturing community because it provides a better understanding of the structure-performance relationship for BOL and degraded PEMFC. Knowing the factors that affect the degradation and their relative effects, appropriate actions can be taken to address the right design parameters in the fabrication of fuel cells, or apply appropriate protective protocols to prevent particular changes.

# CRediT authorship contribution statement

Amir Peyman Soleymani: Visualization, Investigation, Methodology, Data curation, Writing – original draft, Writing – review & editing. Leonard Bonville: Data curation, Validation, Writing – review & editing. Chunmei Wang: Conceptualization, Data curation, Formal analysis, Investigation, Methodology, Software, Validation, Visualization. Stephanie Schaefer: Visualization, Data curation, Writing – review & editing. James Waldecker: Conceptualization, Funding acquisition, Investigation, Methodology, Resources, Supervision, Validation, Writing – review & editing. Jasna Jankovic: Supervision, Funding acquisition, Investigation, Conceptualization, Methodology, Data curation, Writing – review & editing.

#### Declaration of competing interest

The authors declare the following financial interests/personal relationships which may be considered as potential competing interests: Jasna Jankovic reports financial support was provided by National Science Foundation.

#### Data availability

The data that has been used is confidential.

#### Acknowledgment

The authors would like to acknowledge support from NSF CAREER award # 204606: CAREER: Understanding degradation mechanisms in sustainable energy electrochemical systems using advanced characterization approaches, Ford Motor Company for providing the fresh and tested MEAs, and Ms. Marcia Reid at the electron microscopy facility, McMaster University, Canada, for preparation of TEM samples.

# Appendix A. Supplementary data

Supplementary data to this article can be found online at https://doi.org/10.1016/j.jpowsour.2023.232807.

#### References

- Hydrogen and fuel cell technologies office | Department of Energy, (n.d.). https://www.energy.gov/eere/fuelcells/hydrogen-and-fuel-cell-technologies-office (accessed April 16, 2021).
- [2] K. Garsany, Y. Swider-Lyons, Kinetic activity in electrochemical cells, in: Springer Handb. Electrochem. Energy, Springer, Berlin, Heidelberg, 2017, pp. 423–445, https://doi.org/10.1007/978-3-662-46657-5\_14.
- [3] D. Wilkinson, J. Zhang, R. Hui, J. Fergus, X. Li, Proton Exchange Membrane Fuel Cells: Materials Properties and Performance, CRC Press, 2009. https://books.goog le.com/books?hl=en&lr=&id=7euwuMeumk0C&oi=fnd&pg=PP1&dq=pem+fue l+cells+catalysts+book&ots=sPfeRphNaW&sig=TLqdv02GFvOidC riRINbS0ZD50E, accessed April 5, 2020.
- [4] J.P. Owejan, J.J. Gagliardo, J.M. Sergi, S.G. Kandlikar, T.A. Trabold, Water management studies in PEM fuel cells, Part I: fuel cell design and in situ water distributions, Int. J. Hydrogen Energy 34 (2009) 3436–3444, https://doi.org/ 10.1016/j.ijhydene.2008.12.100.
- [5] X.Z. Yuan, H. Wang, PEM fuel cell fundamentals, in: PEM Fuel Cell Electrocatal. Catal. Layers Fundam. Appl., Springer London, 2008, pp. 1–87, https://doi.org/ 10.1007/978-1-84800-936-3\_1.
- [6] T. Reshetenko, V. Laue, U. Krewer, K. Artyushkova, Poisoning effects of sulfur dioxide in an air stream on spatial proton exchange membrane fuel cell performance, J. Power Sources 438 (2019), 226949, https://doi.org/10.1016/j. jpowsour.2019.226949.
- [7] R.L. Borup, A. Kusoglu, K.C. Neyerlin, R. Mukundan, R.K. Ahluwalia, D.A. Cullen, K.L. More, A.Z. Weber, D.J. Myers, Recent developments in catalyst-related PEM fuel cell durability, Curr. Opin. Electrochem. 21 (2020) 192–200, https://doi.org/10.1016/j.coelec.2020.02.007
- [8] A.P. Soleymani, L.R. Parent, J. Jankovic, Challenges and opportunities in understanding proton exchange membrane fuel cell materials degradation using in-

- situ electrochemical liquid cell transmission electron microscopy, Adv. Funct. Mater. 32 (2022), 2105188, https://doi.org/10.1002/ADFM.202105188.
- [9] C.A. Reiser, L. Bregoli, T.W. Patterson, J.S. Yi, J.D. Yang, M.L. Perry, T.D. Jarvi, A reverse-current decay mechanism for fuel cells, Electrochem. Solid State Lett. 8 (2005) A273, https://doi.org/10.1149/1.1896466.
- [10] H. Tang, Z. Qi, M. Ramani, J.F. Elter, PEM fuel cell cathode carbon corrosion due to the formation of air/fuel boundary at the anode, J. Power Sources 158 (2006) 1306–1312, https://doi.org/10.1016/j.jpowsour.2005.10.059.
- [11] E. Guilminot, A. Corcella, F. Charlot, F. Maillard, M. Chatenet, Detection of Pt[sup z+] ions and Pt nanoparticles inside the membrane of a used PEMFC, J. Electrochem. Soc. 154 (2007) B96, https://doi.org/10.1149/1.2388863.
- [12] T. Zhang, P. Wang, H. Chen, P. Pei, A review of automotive proton exchange membrane fuel cell degradation under start-stop operating condition, Appl. Energy 223 (2018) 249–262, https://doi.org/10.1016/J.APENERGY.2018.04.049.
- [13] Y. Yu, H. Li, H. Wang, X.Z. Yuan, G. Wang, M. Pan, A review on performance degradation of proton exchange membrane fuel cells during startup and shutdown processes: causes, consequences, and mitigation strategies, J. Power Sources 205 (2012) 10–23, https://doi.org/10.1016/J.JPOWSOUR.2012.01.059.
- [14] M. Hara, M. Lee, C.H. Liu, B.H. Chen, Y. Yamashita, M. Uchida, H. Uchida, M. Watanabe, Electrochemical and Raman spectroscopic evaluation of Pt/graphitized carbon black catalyst durability for the start/stop operating condition of polymer electrolyte fuel cells, Electrochim. Acta 70 (2012) 171–181, https://doi.org/10.1016/J.ELECTACTA.2012.03.043.
- [15] M. Lee, M. Uchida, K. Okaya, H. Uchida, M. Watanabe, Durability of Pt/graphitized carbon catalyst prepared by the nanocapsule method for the start/stop operating condition of polymer electrolyte fuel cells, Electrochemistry 79 (2011) 381–387, https://doi.org/10.5796/ELECTROCHEMISTRY.79.381.
- [16] Y. Yamashita, S. Itami, J. Takano, M. Kodama, K. Kakinuma, M. Hara, M. Watanabe, M. Uchida, Durability of Pt catalysts supported on graphitized carbon-black during gas-exchange start-up operation similar to that used for fuel cell vehicles, J. Electrochem. Soc. 163 (2016) F644–F650, https://doi.org/ 10.1149/2.0771607JES/XML.
- [17] M. Uchida, K. Kakinuma, A. Iiyama, Evaluation of cell performance and durability for cathode catalysts (platinum supported on carbon blacks or conducting ceramic nanoparticles) during simulated fuel cell vehicle operation: start-up/shutdown cycles and load cycles, Nanostructured Mater. Next-Generation Energy Storage, Convers. Fuel Cells (2018) 53–113, https://doi.org/10.1007/978-3-662-56364-9\_ 3/COVER
- [18] P.T. Yu, F.T. Wagner, Method for mitigating cell degradation due to startup and shutdown va cathode re-circulation combined with electrical shorting of stack, U.S. Patent 9 236 (2017) 614.
- [19] K. More, Microstructural characterization of polymer electrolyte membrane fuel cell (PEMFC) membrane electrode assemblies (MEAs), 2005. http://hydrogen.ener gy.gov/pdfs/progress05/vii\_i\_2\_more.pdf.
- [20] D.M. Fadzillah, M.I. Rosli, M.Z.M. Talib, S.K. Kamarudin, W.R.W. Daud, Review on microstructure modelling of a gas diffusion layer for proton exchange membrane fuel cells, Renew. Sustain. Energy Rev. 77 (2017) 1001–1009, https://doi.org/ 10.1016/J.RSER.2016.11.235
- [21] M. Kang, J. Sim, K. Min, Analysis of performance degradation on the components in polymer electrolyte membrane fuel cell by dissecting the oxygen diffusion region, J. Power Sources 552 (2022), 232236, https://doi.org/10.1016/J. JPOWSOUR.2022.232236.
- [22] S. Waseem, P.H. Maheshwari, P. Maheshwari, A.K. Sahu, A. Saini, S.R. Dhakate, Configuring the porosity and microstructure of carbon paper electrode using pore formers and its influence on the performance of PEMFC, Energy Fuel. 34 (2020) 16736–16745, https://doi.org/10.1021/ACS.ENERGYFUELS.0C02838/ASSET/ IMAGES/LARGE/EF0C02838\_0008.JPEG.
- [23] K. More, R. Borup, K. Reeves, Identifying contributing degradation phenomena in PEM fuel cell membrane electride assemblies via electron microscopy, ECS Trans. 3 (2006) 717–733, https://doi.org/10.1149/1.2356192/XML.
- [24] B.T. Sneed, D.A. Cullen, K.S. Reeves, O.E. Dyck, D.A. Langlois, R. Mukundan, R. L. Borup, K.L. More, 3D analysis of fuel cell electrocatalyst degradation on alternate carbon supports, ACS Appl. Mater. Interfaces 9 (2017) 29839–29848, https://doi.org/10.1021/ACSAMI.7B09716/SUPPL\_FILE/AM7B09716\_SI\_004.AVI.
- [25] P. Saha, K. Khedekar, H. Wang, P. Atanassov, L. Cheng, S. Stewart, C. Johnston, I. V. Zenyuk, Correlating the morphological changes to electrochemical performance during carbon corrosion in polymer electrolyte fuel cells, J. Mater. Chem. A. 10 (2022) 12551–12562, https://doi.org/10.1039/D2TA02666J.
- [26] Y. Qi, Y. Huang, Z. Gao, C.H. Chen, A. Perego, H. Yildirim, M. Odgaard, T. Asset, P. Atanassov, I.V. Zenyuk, Insight into carbon corrosion of different carbon supports for Pt-based electrocatalysts using accelerated stress tests in polymer electrolyte fuel cells, J. Power Sources 551 (2022), 232209, https://doi.org/ 10.1016/J.JPOWSOUR.2022.232209.
- [27] S.K. Babu, R. Mukundan, C. Wang, D. Langlois, D.A. Cullen, D. Papadias, K.L. More, R. Ahluwalia, J. Waldecker, R. Borup, Effect of catalyst and catalyst layer composition on catalyst support durability, J. Electrochem. Soc. 168 (2021), 044502, https://doi.org/10.1149/1945-7111/ABF21F.
- [28] K.L. More, Microstructural characterization of PEM fuel cell MEAs, progress report for the DOE hydrogen program, Prog. Rep. DOE Hydrog. Progr. (2006) 1033–1038.
- [29] M. Wang, J.H. Park, S. Kabir, K.C. Neyerlin, N.N. Kariuki, H. Lv, V.R. Stamenkovic, D.J. Myers, M. Ulsh, S.A. Mauger, Impact of catalyst ink dispersing methodology on fuel cell performance using in-situ X-ray scattering, ACS Appl. Energy Mater. 2 (2019) 6417–6427, https://doi.org/10.1021/ACSAEM.9B01037/ASSET/IMAGES/ LARGE/AE9B01037\_0007\_JPEG.
- [30] C. Lei, F. Yang, N. Macauley, M. Spinetta, G. Purdy, J. Jankovic, D.A. Cullen, K. L. More, Y.S. Kim, H. Xu, Impact of catalyst ink dispersing solvent on PEM fuel cell

- performance and durability, J. Electrochem. Soc. 168 (2021), 044517, https://doi.org/10.1149/1945-7111/ABF2B0.
- [31] F. Rong, C. Huang, Z.S. Liu, D. Song, Q. Wang, Microstructure changes in the catalyst layers of PEM fuel cells induced by load cycling: Part II. Simulation and understanding, J. Power Sources 175 (2008) 712–723, https://doi.org/10.1016/J. PDWSQLIB 2007 10.007
- [32] Q. Meyer, J. Hack, N. Mansor, F. Iacoviello, J.J. Bailey, P.R. Shearing, D.J.L. Brett, Multi-scale imaging of polymer electrolyte fuel cells using X-ray micro- and nanocomputed tomography, transmission electron microscopy and helium-ion microscopy, Fuel Cell. 19 (2019) 35–42, https://doi.org/10.1002/ FUCF.201800047.
- [33] Y. Chen, Y. Singh, D. Ramani, F.P. Orfino, M. Dutta, E. Kjeang, 4D imaging of chemo-mechanical membrane degradation in polymer electrolyte fuel cells - Part 1: understanding and evading edge failures, J. Power Sources 520 (2022), 230674, https://doi.org/10.1016/J.JPOWSOUR.2021.230674.
- [34] L. Hu, T. Van Cleve, H. Yu, J.H. Park, N. Kariuki, A.J. Kropf, R. Mukundan, D. A. Cullen, D.J. Myers, K.C. Neyerlin, Electrochemical characterization of evolving ionomer/electrocatalyst interactions throughout accelerated stress tests, J. Power Sources 556 (2023), 232490, https://doi.org/10.1016/J. J.POWSOUR 2022 232490
- [35] P.J. Ferreira, G.J. la O', Y. Shao-Horn, D. Morgan, R. Makharia, S. Kocha, H. A. Gasteiger, Instability of Pt/C electrocatalysts in proton exchange membrane fuel cells, J. Electrochem. Soc. 152 (2005) A2256, https://doi.org/10.1149/1.2050347.
- [36] E. Guilminot, A. Corcella, M. Chatenet, F. Maillard, F. Charlot, G. Berthomé, C. Iojoiu, J.-Y. Sanchez, E. Rossinot, E. Claude, Membrane and active layer degradation upon PEMFC steady-state operation: I. Platinum dissolution and redistribution within the MEA, J. Electrochem. Soc. 154 (2007) B1106, https://doi. org/10.1149/1.2775218;XMI.
- [37] L. Dubau, J. Durst, F. Maillard, M. Chatenet, J. André, E. Rossinot, Heterogeneities of aging within a PEMFC MEA, Fuel Cell. 12 (2012) 188–198, https://doi.org/ 10.1002/FUCE.201100073.
- [38] L. Dubau, F. Maillard, M. Chatenet, L. Guetaz, J. André, E. Rossinot, Durability of Pt[sub 3]Co/C cathodes in a 16 cell PEMFC stack: macro/microstructural changes and degradation mechanisms, J. Electrochem. Soc. 157 (2010) B1887, https://doi. org/10.1149/1.3485104/XML.
- [39] J. Zhao, S. Shahgaldi, X. Li, Z. (Simon) Liu, Experimental observations of microstructure changes in the catalyst layers of proton exchange membrane fuel cells under wet-dry cycles, J. Electrochem. Soc. 165 (2018) F3337–F3345, https://doi.org/10.1149/2.0391806JES/XML.
- [40] S.Y. Lee, H.J. Kim, E. Cho, K.S. Lee, T.H. Lim, I.C. Hwang, J.H. Jang, Performance degradation and microstructure changes in freeze–thaw cycling for PEMFC MEAs with various initial microstructures, Int. J. Hydrogen Energy 35 (2010) 12888–12896, https://doi.org/10.1016/J.IJHYDENE.2010.08.070.
- [41] J.P. Braaten, S. Ogawa, V. Yarlagadda, A. Kongkanand, S. Litster, Studying Pt-based fuel cell electrode degradation with nanoscale X-ray computed tomography, J. Power Sources 478 (2020), 229049, https://doi.org/10.1016/J. JPOWSOUR.2020.229049.
- [42] S.F. Zaccarine, M. Shviro, J.N. Weker, M.J. Dzara, J. Foster, M. Carmo, S. Pylypenko, Multi-scale multi-technique characterization approach for analysis of PEM electrolyzer catalyst layer degradation, J. Electrochem. Soc. 169 (2022), 064502. https://doi.org/10.1149/1945-7111/AC7258.
- [43] A. Kneer, J. Jankovic, D. Susac, A. Putz, N. Wagner, M. Sabharwal, M. Secanell, Correlation of changes in electrochemical and structural parameters due to voltage cycling induced degradation in PEM fuel cells, J. Electrochem. Soc. 165 (2018) F3241–F3250, https://doi.org/10.1149/2.0271806jes.
- [44] N. Macauley, R.D. Lousenberg, M. Spinetta, S. Zhong, F. Yang, W. Judge, V. Nikitin, A. Perego, Y. Qi, S. Pedram, J. Jankovic, I.V. Zenyuk, H. Xu, Highly durable fluorinated high oxygen permeability ionomers for proton exchange membrane fuel cells, Adv. Energy Mater. 12 (2022), 2201063, https://doi.org/ 10.1002/AFNM.202201063.
- [45] C. Wang, M. Ricketts, A.P. Soleymani, J. Jankovic, J. Waldecker, J. Chen, Effect of carbon support characteristics on fuel cell durability in accelerated stress testing, J. Electrochem. Soc. 168 (2021), 044507, https://doi.org/10.1149/1945-7111/ abf265.
- [46] C. Wang, M. Ricketts, A.P. Soleymani, J. Jankovic, J. Waldecker, J. Chen, C. Xu, Improved carbon corrosion and platinum dissolution durability in automotive fuel cell startup and shutdown operation, J. Electrochem. Soc. 168 (2021), 034503, https://doi.org/10.1149/1945-7111/ABE6EA.
- [47] US DRIVE fuel cell technical team roadmap | Department of Energy, (n.d.). https://www.energy.gov/eere/vehicles/downloads/us-drive-fuel-cell-technical-team-roadmap (accessed November 25, 2022).
- [48] M. El Hannach, T. Soboleva, K. Malek, A.A. Franco, M. Prat, J. Pauchet, S. Holdcroft, Characterization of pore network structure in catalyst layers of polymer electrolyte fuel cells, J. Power Sources 247 (2014) 322–326, https://doi. org/10.1016/j.jpowsour.2013.08.049.
- [49] M. Watanabe, D.B. Williams, The quantitative analysis of thin specimens: a review of progress from the Cliff-Lorimer to the new zeta-factor methods, J. Microsc. 221 (2006) 89–109, https://doi.org/10.1111/j.1365-2818.2006.01549.x.
- [50] A.P. Soleymani, A comprehensive microscopy approach toward proton exchange membrane fuel cell degradation, University of Connecticut, 2022 n.d, https://col ections.ctdigitalarchive.org/islandora/object/20002:860707096. accessed September 26, 2022.
- [51] L.M. Roen, C.H. Paik, T.D. Jarvi, Electrocatalytic corrosion of carbon support in PEMFC cathodes, Electrochem. Solid State Lett. 7 (2004) A19, https://doi.org/ 10.1149/1.1630412.

- [52] T. Mittermeier, A. Weiß, F. Hasché, G. Hübner, H.A. Gasteiger, PEM fuel cell start-up/shut-down losses vs temperature for non-graphitized and graphitized cathode carbon supports, J. Electrochem. Soc. 164 (2017) F127–F137, https://doi.org/10.1149/2.1061702JES/XML.
- [53] J. Zhao, X. Huang, H. Chang, S. Hwa Chan, Z. Tu, Effects of operating temperature on the carbon corrosion in a proton exchange membrane fuel cell under high current density, Energy Convers. Manag. X. 10 (2021), 100087, https://doi.org/ 10.1016/J.ECMX.2021.100087.
- [54] W. Bi, G.E. Gray, T.F. Fuller, PEM fuel cell PtC dissolution and deposition in nafion electrolyte, Electrochem. Solid State Lett. 10 (2007) 101–104, https://doi.org/ 10.1149/1.2712796.
- [55] C.K. Mittelsteadt, H. Liu, Conductivity, permeability, and ohmic shorting of ionomeric membranes, in: Handb. Fuel Cells, John Wiley & Sons, Ltd, 2010, https://doi.org/10.1002/9780470974001.F500025.
- [56] P. Nen, P. Pei, Y. Li, Z. Wu, D. Chen, S. Huang, Degradation mechanisms of proton exchange membrane fuel cell under typical automotive operating conditions, Prog. Energy Combust. Sci. 80 (2020), 100859, https://doi.org/10.1016/j. pecs.2020.100859.
- [57] P. Schneider, C. Sadeler, A.-C. Scherzer, N. Zamel, D. Gerteisen, Fast and reliable state-of-health model of a PEM cathode catalyst layer, J. Electrochem. Soc. 166 (2019) F322–F333, https://doi.org/10.1149/2.0881904JES/XML.

- [58] S.C. Ball, S.L. Hudson, B.R. Theobald, D. Thompsett, PtCo, a durable catalyst for automotive PEMFC? ECS Trans. 11 (2007) 1267, https://doi.org/10.1149/ 1.2781040
- [59] R. DeHoff, Thermodynamics in Materials Science, CRC Press, 2006. https://books.google.com/books?hl=en&lr=&id=-uOEiGJDmxIC&oi=fnd&pg=PP1&dq=Thermodynamics-in-Materials-Science-dehoff&ots=Q4\_uKQvb71&sig=klzjtcJ0ydPiLc8fyNiaLqPbo3c. May 21, 2022.
- [60] J. Dillet, D. Spernjak, A. Lamibrac, G. Maranzana, R. Mukundan, J. Fairweather, S. Didierjean, R.L. Borup, O. Lottin, Impact of flow rates and electrode specifications on degradations during repeated startups and shutdowns in polymerelectrolyte membrane fuel cells, J. Power Sources 250 (2014) 68–79, https://doi. org/10.1016/j.jpowsour.2013.10.141.
- [61] J. Marie, R. Chenitz, M. Chatenet, S. Berthon-Fabry, N. Cornet, P. Achard, Highly porous PEM fuel cell cathodes based on low density carbon aerogels as Pt-support: experimental study of the mass-transport losses, J. Power Sources 190 (2009) 423–434, https://doi.org/10.1016/J.JPOWSOUR.2009.01.047.
- [62] A.P. Soleymani, M. Reid, J. Jankovic, An epoxy-free sample preparation approach to enable imaging of ionomer and carbon in polymer electrolyte membrane fuel cells, Adv. Funct. Mater. 33 (2023), 2209733, https://doi.org/10.1002/ ADFM.202209733.